

NON-GAUSSIANITY DUE TO POSSIBLE RESIDUAL FOREGROUND SIGNALS IN WILKINSON MICROWAVE ANISOTROPY PROBE FIRST-YEAR DATA USING SPHERICAL WAVELET APPROACHES

XIN LIU¹ AND SHUANG NAN ZHANG^{1,2,3,4}

Draft version November 15, 2018

ABSTRACT

We perform multi-scale non-Gaussianity detection and localization to the *Wilkinson Microwave Anisotropy Probe* (WMAP) first-year data in both wavelet and real spaces. Such an analysis is facilitated by spherical wavelet transform and inverse transform techniques developed by the YAWtb team. Skewness and kurtosis as test statistics are calculated on scales from about 1° to 30° on the sky as well as toward different directions using anisotropic spherical Morlet wavelet (SMW). A maximum deviation from Gaussian simulations with a right tail probability of $\sim 99.9\%$ is detected at an angular scale of $\sim 12^\circ$ at an azimuthal orientation of $\sim 0^\circ$ on the sky. In addition, some significant non-Gaussian spots have been identified and localized in real space from both the combined Q-V-W map recommended by the WMAP team and the Tegmark foreground-cleaned map. Systematic effects due to beams and noise can be rejected as the source of this non-Gaussianity. Several tests show that residual foreground contamination may significantly contribute to this non-Gaussian feature. It is thus still premature to do more precise tests on the non-Gaussianity of the intrinsic CMB fluctuations before we can identify the origin of these foreground signals, understand their nature, and finally remove them from the CMB maps completely.

Subject headings: cosmic microwave background — methods: data analysis

1. INTRODUCTION

Since the release of the *Wilkinson Microwave Anisotropy Probe* (WMAP) first-year data, much work has been done to investigate the properties of whole-sky cosmic microwave background (CMB) anisotropies with high resolution and sensitivity (Bennett *et al.* 2003a; Hinshaw *et al.* 2003a,b). The currently favored Λ CDM model is based on the assumption of Gaussian initial fluctuations generated by inflation, which result in Gaussian temperature anisotropies in the CMB (Guth & Pi 1982; Hawking 1982; Bardeen, Steinhardt & Turner 1983). Thus the test of non-Gaussianity of CMB temperature anisotropies provides us an important constraint on distinguishing theories of the origin of primordial fluctuations. In addition, the issue is also fundamental for the determination of cosmological parameters in the framework of the inflation paradigm, since they can only be determined correctly from the angular power spectrum if the CMB temperature anisotropies constitute a Gaussian random field (Bardeen *et al.* 1986; Bond & Efstathiou 1987).

Many efforts have been made to test the CMB anisotropy, and some of them found that the WMAP data are consistent with Gaussian primordial fluctuations (Komatsu *et al.* 2003; Colley *et al.* 2003; Gaztañaga & Wagg 2003; Gaztañaga *et al.* 2003), whereas some de-

tected non-Gaussianity using various approaches (Coles *et al.* 2004; Chiang *et al.* 2003; Chiang & Naselsky 2004; Park 2004; Eriksen *et al.* 2004a, 2004b; Larson & Wandelt 2004; Vielva *et al.* 2004; Hansen *et al.* 2004; Mukherjee & Wang 2004; McEwen *et al.* 2005; Wibig & Wolfendale 2005). Non-standard inflationary models and various cosmic defects could lead to non-Gaussian primordial CMB fluctuations. Non-Gaussianity could also be introduced by secondary effects, such as the integrated Sachs-Wolfe effect, the Rees-Sciama effect, the Sunyaev-Zel'dovich effect and gravitational lensing, or by measurement systematics, foreground and noise. Recent reports found residuals, or systematic effects correction, as the source of non-Gaussianity (Chiang *et al.* 2003; Chiang & Naselsky 2004; Naselsky *et al.* 2003, 2004; Eriksen *et al.* 2004b; Hansen *et al.* 2004; Wibig & Wolfendale 2005). Thus, foreground removal should be dealt with care before any conclusions on the statistical properties of the CMB anisotropies are reached. Meanwhile, the WMAP team derived a foreground template that is of great importance for accurately understanding the Galactic foreground emissions.

In this paper, we perform the non-Gaussianity test on WMAP first-year data and investigate the possible sources of the detected non-Gaussianity, especially residual foreground emissions, using spherical wavelet approaches. Wavelets are very useful for data analysis due to their nature of space-frequency localization. They have already been applied to the *Cosmic Background Explorer* (COBE)-Differential Microwave Radiometer (DMR) data (Pando *et al.* 1998; Mukherjee *et al.* 2000; Aghanim *et al.* 2001; Tenorio *et al.* 1999; Barreiro *et al.* 2000; Cayón *et al.* 2001), as well as the WMAP first-year data (Mukherjee & Wang, 2004; Vielva *et al.* 2004; McEwen *et al.* 2005), using the non-Gaussianity test in wavelet space. We perform the

¹ Physics Department and Tsinghua Center for Astrophysics, Tsinghua University, Beijing 100084, China; liux00@mails.tsinghua.edu.cn, zhangsn@tsinghua.edu.cn.

² Key Laboratory of Particle Astrophysics, Institute of High Energy Physics, Chinese Academy of Sciences, P.O. Box 918-3, Beijing 100039, China

³ Physics Department, University of Alabama in Huntsville, Huntsville, AL 35899, USA

⁴ Space Science Laboratory, NASA Marshall Space Flight Center, SD50, Huntsville, AL 35812, USA

analysis in both wavelet and real spaces using various wavelet bases. The paper is organized as follows. In § 2, we briefly review the general theory of spherical wavelets and its implementation. In § 3, we describe how the data are processed and analyzed for the non-Gaussianity test with spherical wavelet approaches. Results of the test and discussions of possible sources of the detected non-Gaussianity are presented in § 4. We conclude and discuss our results further in § 5.

2. WAVELETS ON THE SPHERE

Wavelet approaches are very powerful for detecting non-Gaussianity in CMB data (Hobson *et al.* 1999; Martínez-González *et al.* 2002). Due to the special nature of wavelets, a multi-scale analysis can be done to amplify any non-Gaussian features dominating at some specific scales. Analyzing full-sky CMB features involves data on spherical manifolds, which require a wavelet approach on the sphere. We consider the continuous spherical wavelet transform (CSWT), initially proposed by Antoine & Vandergheynst (1998), based on group theory principles, and the framed spherical wavelet transform (FSWT), implemented by the Yet Another Wavelet toolbox (YAWtb⁵) team. In this section we briefly review the general theory of CSWT. We use CSWT for the non-Gaussianity detection in wavelet space; for filtering non-Gaussian spots in real space, we use FSWT and inverse FSWT, where the theory of frames is only useful when the inverse transform is carried out. Since FSWT is based on CSWT and the theory of frames is too technical to be stated in detail here, the paper by Bogdanova I. *et al.* (2004) should be referenced for details. For general readers who want to reproduce our results, they can use `fwtsph.m` and `ifwtsph.m` in the YAWtb for FSWT and inverse FSWT, respectively.

2.1. The General Theory

The CSWT, like Euclidean counterpart, is based on affine transformations. On the two-dimensional sphere S^2 , the basic operations are represented by the following unitary operators (Bogdanova *et al.* 2004):

- *Rigid rotation* R_ρ , where ρ is an element of the group of rotations $SO(3)$, may be parameterized in terms of its Euler angles $\omega \equiv (\theta, \varphi)$ by

$$(R_\rho f)(\omega) = f(\rho^{-1}\omega), \quad (1)$$

where $\theta \in [0, \pi]$, $\varphi \in [0, 2\pi)$, f is an operator, and ρ^{-1} is the opposite operator of ρ in the group of rotations $SO(3)$.

- *Conformal dilation* D_a , with scale $a \in \mathbb{R}^+$:

$$(D_a f)(\omega) = \lambda(a, \theta)^{1/2} f(\omega_{1/a}), \quad (2)$$

where \mathbb{R}^+ is the set of positive real numbers, $\omega_a \equiv (\theta_a, \varphi)$, and the corresponding dilation size on the sky is given by

$$\tan \frac{\theta_a}{2} = a \tan \frac{\theta}{2}, \quad (3)$$

where λ is a normalization factor which is given by

$$\lambda(a, \theta) = \frac{4a^2}{[(a^2 - 1) \cos \theta + (a^2 + 1)]^2}. \quad (4)$$

⁵ Yet Another Wavelet toolbox. See the YAWtb homepage (<http://www.fyma.ucl.ac.be/projects/yawtb>) for more information.

A set of wavelet basis on the sphere is constructed by rotations and dilations of an admissible mother spherical wavelet $\psi \in L^2(S^2)$. The corresponding wavelet family $\{\psi_{a,\rho} \equiv R_\rho D_a \psi\}$ provides an over-complete set of functions in $L^2(S^2)$. The CSWT is given by the projection onto each wavelet basis function in the usual manner,

$$(CSWT_\psi f)(a, \omega) = \int_{S^2} d\mu(\omega') (R_\omega \psi_a)^*(\omega') f(\omega'), \quad (5)$$

where $*$ denotes complex conjugation and $d\mu(\omega) = \sin \theta d\theta d\varphi$ is the rotation-invariant measure on the sphere.

2.2. Practical Implementation

The YAWtb team has developed the fast algorithm of CSWT and FSWT that they integrated into the Matlab YAWtb toolbox. The scales are discretized as

$$a \in A = \{a_j \in \mathbb{R}^+ : a_j < a_{j+1}, j \in Z\}, \quad (6)$$

where j is the scale parameter. We work on data discretized on the equi-angular grid \mathcal{G}_B defined by:

$$\mathcal{G}_B \equiv \{(\theta_p, \varphi_q) : p, q \in Z[2B]\}, \quad (7)$$

where the positive integer B is the resolution parameter, $Z[2B] = \{0, \dots, 2B - 1\}$, $\theta_p = (2p + 1)\pi/4B$ and $\varphi_q = q\pi/B$. The positions are indexed by the scale level, related to the scale in such a way that $\omega \in \mathcal{G}_{B_j}$, with

$$\mathcal{G}_{B_j} = \{(\theta_{jp}, \varphi_{jq}) \in S^2 : \theta_{jp} = \frac{(2p + 1)\pi}{4B_j}, \phi_{jq} = \frac{q\pi}{B_j}\}, \quad (8)$$

where $B_j \in Z[2B]$.

2.3. Spherical Wavelet Basis

The wavelet is said to be *isotropic* if it does not depend on φ when centered at the north pole. In this work we mainly use two different spherical mother wavelets, i.e., the isotropic spherical Mexican hat wavelet (SMHW) and anisotropic spherical Morlet wavelet (SMW), where anisotropic means the wavelet is not only a function of θ but also a function of φ . We have also performed the analysis using the difference of Gaussians (DOG) wavelet (Bogdanova I. *et al.* 2004), the result of which is almost identical to that using the SMHW. The SMHW has been considered the best for the detection of non-Gaussian signatures with spherical symmetry. It has already been applied to non-Gaussian studies of the COBE-DMR data (Cayón *et al.* 2001, 2003), Planck simulations (Martínez-González *et al.* 2002) and the WMAP first-year data (Mukherjee & Wang, 2004; Vielva *et al.* 2004; McEwen *et al.* 2005). However, it is not so sensitive for the detection of anisotropic non-Gaussianity (McEwen *et al.* 2005). We adopt the SMW for the non-Gaussianity detection and the SMHW for localization. The mother SMW wavelet is given by

$$\Psi_M(\theta, \varphi) = \frac{e^{ik_0 \tan(\theta/2) \cos(\varphi_0 - \varphi)} e^{-(1/2) \tan^2(\theta/2)}}{(1 + \cos \theta)^2}, \quad (9)$$

where k_0 is the projection of the wave vector of the wavelet and φ_0 is the rotation parameter reflecting directional features. As defined in Martínez-González *et al.* (2002), the SMHW is given by

$$\Psi_{MH}(\theta, a) = \frac{1}{\sqrt{2\pi}N(a)} \left[1 + \left(\frac{y}{2}\right)^2\right]^2 \left[2 - \left(\frac{y}{a}\right)^2\right] e^{-y^2/2a^2}, \quad (10)$$

where $y \equiv 2 \tan(\theta/2)$ and $N(a) \equiv a(1 + a^2/2 + a^4/4)^{1/2}$ is a normalization constant.

3. NON-GAUSSIANITY ANALYSIS

Spherical anisotropic wavelet analysis is applied to probe the *WMAP* first-year data for possible deviations from Gaussianity. We follow a strategy similar to that of Vielva *et al.* (2004) and McEwen *et al.* (2005), whereas our pixelisation of the data onto the sphere and the treatment of masks are different from theirs.

3.1. Data Pipeline

We adopt the same data set analyzed by Komatsu *et al.* 2003 and Vielva *et al.* 2004 in their non-Gaussianity studies. The CMB-dominated bands (two Q-band maps at 40.7 GHz, two V-band maps at 60.8 GHz, and four W-band maps at 93.5 GHz) are combined to give a map with the signal-to-noise ratio enhanced. All these maps with receiver noise, as well as beam properties, are available from the Legacy Archive for Microwave Background Data Analysis (LAMBDA) Web site.⁶ These maps are provided in the HEALPix (Górski *et al.* 1999) format at a resolution of $N_{side} = 512$. The number of pixels in a HEALPix map is given by $12N_{side}^2$. We project these data in the HEALPix pixelisation onto the equi-angular spherical grid \mathcal{G}_B , where $B = 256$ with the individual noise weight as defined below, in order that the data set be suitable for matrix computation. The surface of the sphere is redivided by the equiangular spherical grid, and then the data are projected into the grid according to their position and recombined within each grid to give a weighted average in the new pixelisation. Note that pixels in the new representation do not have equal areas, but this is suitable for the inverse FSWT, where matrix manipulation is used for the fast Fourier algorithm, greatly saving the computation time. Any concern that the transformation can somehow introduce some non-Gaussian features can be alleviated, since the simulation has been done in the same pipeline. The transformed data are of the size 512×512 pixels at a loss of resolution that does not matter in this analysis, since very small scales are dominated by the noise.

At a given position ω of the sky, the thermodynamic temperature is given by

$$T(\omega) = \sum_{j=3}^{10} T_j(\omega) w_j(\omega), \quad (11)$$

where the indices $j = 3$ and 4 refer to the Q-band receivers, $j = 5$ and 6 to the ones of the V-band and $j = 7, 8, 9$ and 10 to the receivers of the W-band (The indices $j = 1$ and 2 are used for the K and Ka receivers, respectively, which are excluded from the analysis.) The noise weight $w_j(\omega)$ is defined by

$$w_j(\omega) = \frac{\bar{w}_j(\omega)}{\sum_{j=3}^{10} \bar{w}_j(\omega)}, \quad \bar{w}_j(\omega) = \frac{N_j(\omega)}{\sigma_{0j}^2} \quad (12)$$

where σ_{0j} is the standard deviation of the receiver noise and $N_j(\omega)$ is the number of observations made by the receiver j at position ω on the sky (Bennett *et al.* 2003a). According to equation (11) and (12), the beams for each of the WMAP channels are different and the noise variances differ from each other, which may potentially create spatially varying beams on the sky. However, these

effects are subdominant to the scales of interest in this paper and can be calibrated out by separate simulations of each band.

Although the maps at selected frequencies are dominated by CMB, Galactic foregrounds (i.e., thermal dust, free-free and synchrotron radiations), as well as extragalactic point sources all contribute significantly to the map. The WMAP team performed a foreground template fit to avoid the Galactic emissions (Bennett *et al.* 2003b): the 94 GHz dust map of Finkbeiner *et al.* (1999) is used as the thermal dust template, the H_α map of Finkbeiner (2003) corrected for extinction through the E_{B-V} map of Schlegel *et al.* (1998) is used as the free-free template, and finally, the synchrotron template is the 408 MHz Haslam *et al.* (1982) map. Hence, equation (11) is modified as

$$\hat{T}(\omega) = \sum_{j=3}^{10} \hat{T}_j(\omega) w_j(\omega), \quad (13)$$

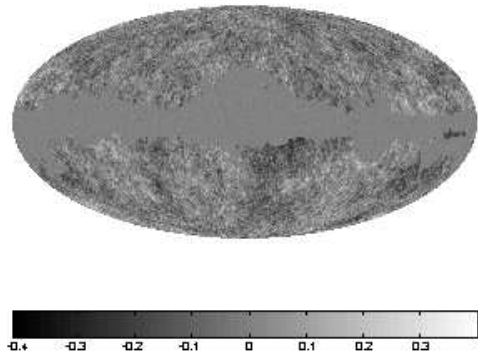
where $\hat{T}_j(\omega)$ is the temperature at position ω for the receiver j after the foreground correction. Foreground-cleaned maps used in this analysis are available from the LAMBDA Web site.

An independent foreground analysis of the *WMAP* first-year data was performed by Tegmark *et al.* (2003). The Tegmark cleaned map is constructed from a linear combination of different band maps with the weights varying over both position and scale. We also perform the analysis on this map in both wavelet and real spaces.

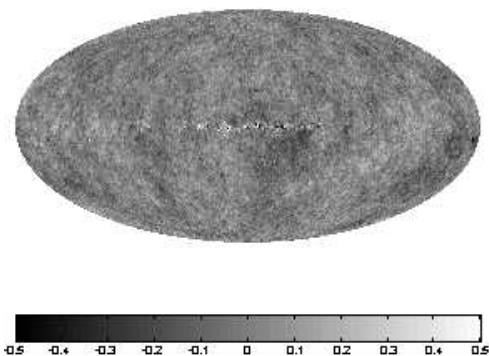
3.2. Mask Treatment

Strong emissions at the Galactic plane and known radio point sources could contaminate any intrinsic features so they should be excluded from the map. Here we adopt the most conservative mask called “Kp0”, which retains 76.8% of the sky. This exclusion may introduce edge effect to the map caused by the zero value of the mask. Generally there are two ways to solve this edge problem. One is to exclude the data near the edges, which has been adopted recently (Mukherjee & Wang 2004; Vielva *et al.* 2004; McEwen *et al.* 2004), although any meaningful CMB features near the edge could have been smeared out. Here we take another approach by filling Gaussian noise in the excluded areas instead of the zero value in order that they do not contribute to deviation from Gaussianity. Pixel noise can be evaluated from N_{obs} via $\sigma = \sigma_{0j}/\sqrt{N_{obs}}$, where σ_{0j} is the standard deviation of the receiver noise of assembly j . Due to the good localization nature of wavelet in both scale and position spaces, we assume that they will not introduce significant correlation to signals in other areas either, which have been tested from the filtering maps such that the filtered cold and hot spots are not caused by particular masks and there is no correlation between these spots and the point sources. Note that the non-Gaussian detection is quite insensitive to the particular choice of the exclusion masks (Mukherjee & Wang, 2004; Vielva *et al.* 2004; McEwen *et al.* 2005). This approach should not introduce non-Gaussian signals, especially at the scales we are interested in this work. The final preprocessed Q-V-W-combined WMAP team map and the Tegmark cleaned map are shown in Fig. 1.

⁶ <http://cmbdata.gsfc.nasa.gov/>



(a) preprocessed combined WMAP team map



(b) preprocessed Tegmark cleaned map

FIG. 1.— CMB temperature anisotropy maps preprocessed from the WMAP team map and the Tegmark cleaned map to be analyzed in this non-Gaussianity study. All maps in this paper are plotted in Galactic coordinates with the Galactic center $(l, b) = (0, 0)$ in the middle and Galactic longitude l increasing to the left.

3.3. Non-Gaussianity Statistics

The wavelet transform is a linear operation, hence the wavelet coefficients of a Gaussian signal will also obey a Gaussian distribution. So we can probe a full-sky map for non-Gaussianity either by looking for deviations from Gaussianity in wavelet space or in real space. We thus examine non-Gaussian features in wavelet space and then localize them in real space. In wavelet space the localization can only be done at a specific scale, whereas in real space using the inverse framed wavelet transform technique, one can localize any deviations of Gaussianity within some scale ranges that would be more natural for the real signals. This is because a map obtained from the inverse framed wavelet transform for a range of scales is equivalent to filtering the original map with a band-pass filter; normally artifacts or spurious oscillations will be produced in a filtered map if the bandwidth is too narrow.

At a given scale (a) , we use the third and fourth moments about the mean as non-Gaussian estimators for the test, i.e., skewness $(S(a))$ and excess kurtosis $(K(a))$

given by:

$$S(a) = \frac{1}{N_a} \sum_{i=1}^{N_a} w_i(a)^3 / \sigma(a)^3 \quad (14)$$

$$K(a) = \frac{1}{N_a} \sum_{i=1}^{N_a} w_i(a)^4 / \sigma(a)^4 - 3, \quad (15)$$

where N_a is the number of coefficients and $\sigma(a)$ is the standard deviation of the wavelet coefficients on scale a .

For a Gaussian distribution, the statistics $S(a)$ and $K(a)$ have zero mean value at each scale a . Thus deviations from zero value in these statistics will indicate the existence of non-Gaussianity in the spherical wavelet coefficients and hence in the corresponding real map.

In the wavelet space we perform the CWT at scales $a \in [0.02, 0.05]$ corresponding to about $(1^\circ, 30^\circ)$ on the sky, as well as within a range of directions $\varphi_0 \in [0^\circ, 360^\circ)$ with a 30° interval. To localize any expected non-Gaussian features, we perform the FSWT (`fwtsph.m` in the YAWtb) and the inverse FSWT (`ifwtsph.m` in the YAWtb) in order to filter the signal through some ranges of scales rather than only at a certain scale. Scales larger than about 3° on the sky are selected because the previous tests in wavelet space only found non-Gaussianity on such scales (Mukherjee & Wang 2004; Vielva *et al.* 2004; McEwen *et al.* 2005). This is the first spherical inverse wavelet analysis applied to the CMB data in which the frame technique is essential.

3.4. Monte Carlo Simulations

Monte Carlo simulations are performed to construct confidence levels for the non-Gaussianity test statistics described above. First, using CMBFAST (Seljak & Zaldarriaga 1996), we calculated the power spectrum C_l using the cosmological parameters estimated by the WMAP team (Spergel *et al.* 2003). Second, 10,000 Gaussian CMB realizations are produced and convolved at each of the WMAP receivers with beam functions. Third, we transform the simulated data from harmonic to real space and add Gaussian noise according to the number of observations per pixel and the noise standard deviation per observation. Finally, all the maps from the eight receivers are combined following equation (13). Monte Carlo simulations of beams and the foreground where the CMB signal is almost negligible are also performed separately in a similar way.

Since the weights used to construct the Tegmark cleaned map differ from those used by the WMAP team, we should carry out other Gaussian simulations strictly following the Tegmark construction method. However, there is no simple way of estimating the noise in each pixel, since much of the noise is due to residual foregrounds, which vary strongly across the sky and are thus correlated between pixels. Thus, Gaussian simulations of the Q-V-W-combined map are also used for the Tegmark map, since for both of the two maps, the weights sum to unity, and we assume that the slight difference in the linear combination of maps should not cause significant changes in the Gaussian confidence levels (McEwen *et al.* 2005).

4. RESULTS

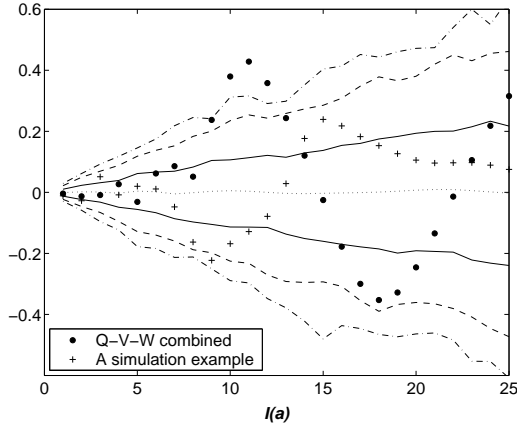
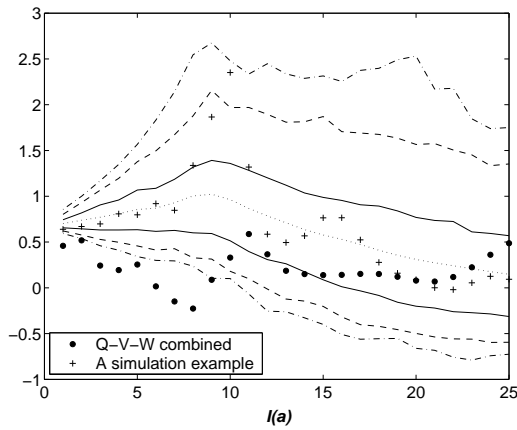
(a) skewness $S(a)$ (b) kurtosis $K(a)$

FIG. 2.— Skewness and kurtosis values of the SMW analysis convolved with the Q-V-W combined WMAP map are shown as filled circles. Here and throughout, the acceptance intervals at the 68% (solid lines), 95% (dashed lines) and 99% (dash-dotted lines) significance levels given by 10,000 Monte Carlo simulations are shown. Note that the error bars are too small compared to the coefficients values and can be ignored in the figures. The values from one example of the simulated Gaussian maps (plus signs) are also shown for comparison. Index $I(a) \equiv 50a$ and the corresponding size on the sky can be obtained from Eqn. (3), where scale index 1 corresponds to 1.15° . Note that only the values obtained from the azimuthal orientation $\varphi_0 \sim 0^\circ$ (i.e., corresponding to the maximum deviations from Gaussianity) are shown.

Analysis in wavelet space has been performed on both of the Q-V-W-combined WMAP map (here and throughout, all CMB maps used are foreground-removed maps) and the Tegmark cleaned map to test the non-Gaussianity in the WMAP first-year data. We also investigate the possible sources of the detected non-Gaussianity. Real space analysis is performed to localize possible deviations over some ranges of scales on the sky.

4.1. Spherical Wavelet Coefficient Statistics

For the Q-V-W-combined WMAP map, the skewness and kurtosis of the wavelet coefficients at different scales

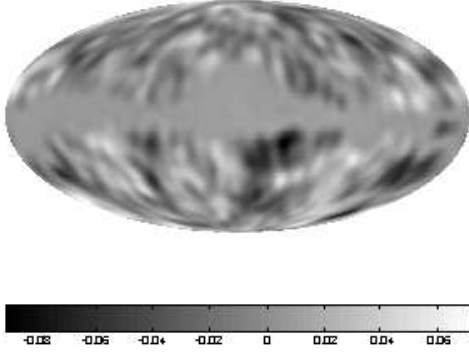
TABLE 1. DEVIATIONS AND SIGNIFICANCE LEVELS OF SPHERICAL WAVELET COEFFICIENT STATISTICS OBTAINED FROM ANALYZING THE Q-V-W COMBINED WMAP MAP. SIGNIFICANT LEVELS ARE CALCULATED FROM 10,000 GAUSSIAN SIMULATIONS. THE NUMBER OF STANDARD DEVIATIONS THE OBSERVATION DEVIATES FROM THE MEAN IS GIVEN BY N_σ ; THE CORRESPONDING SIGNIFICANCE LEVEL OF THE DETECTED NON-GAUSSIANITY IS GIVEN BY δ .

Skewness			Kurtosis		
$I(a)$	N_σ	δ	$I(a)$	N_σ	δ
10	3.31	99.88%	3	-3.77	99.88%
11	3.49	99.79%	4	-3.45	99.65%
12	2.84	99.61%	6	-3.17	98.90%
			7	-3.38	99.21%
			8	-3.01	98.52%

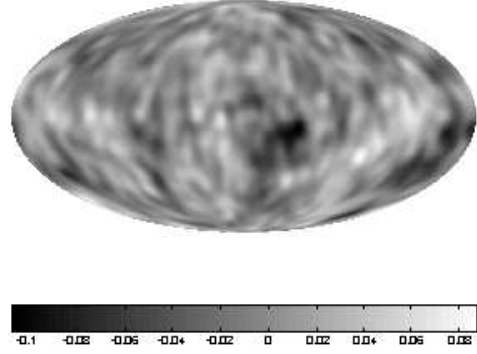
are illustrated in Fig. 2; only the values obtained from the orientation corresponding to the maximum deviations from Gaussianity are shown. Deviations from Gaussianity are detected in both the skewness and kurtosis of the combined map. The numbers of deviations and the corresponding significance levels obtained from 10,000 Gaussian simulations are displayed in Table (1). Since we have tested that deviations using SMW in certain directions are larger than those using SMHW (McEwen *et al.* 2005), we only present the SMW results here. In the skewness, deviations are detected on scales $a_{10} \sim 11^\circ.42$ to $a_{12} \sim 13^\circ.69$, with a maximum around the scale $a_{11} \sim 12^\circ.55$ at a significance level of $> 99\%$. In the kurtosis, deviations are also detected on scales $< a_9 \sim 10^\circ.29$ with a maximum around the scale $a_8 \sim 9^\circ.14$, showing some consistency with the kurtosis test in Vielva *et al.* (2004). Note that a_8 , a_{10} , a_{11} , and a_{12} are scale parameters defined in equation (6) that are related to physical scales according to equation (3).

4.2. Non-Gaussianity Localization

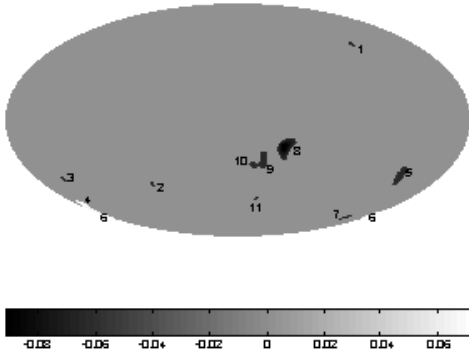
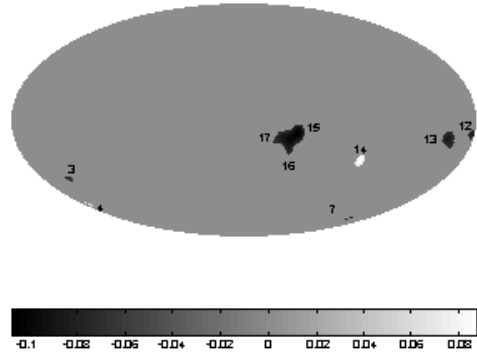
Here we only present results obtained from the isotropic SMHW analysis in real space, since anisotropic SMW will focus only on some signals at a certain direction on the sky. After filtering the map through certain scales, the 3σ threshold filter bank is performed so that only the values of which the absolutes are larger than the threshold value are preserved. Results of this analysis for both the Q-V-W-combined WMAP and the Tegmark cleaned maps are shown in Figs. 3 and 4. Coordinates of the filtered non-Gaussian spots in both maps and their corresponding numbers of deviations are listed in Table (2). Our preliminary work does not reveal any obvious correlation with known sources, although currently we cannot exclude this possibility. Clearly, extensive further work is required. Meanwhile, the filtering results provide some clues for unknown foreground components, which is another aim of our work. Some of the spots are only detected either in the combined WMAP map or in the Tegmark cleaned map, and some spots are seen in both maps, i.e., spots 3, 4, and 7. Note that all the spots found in the Tegmark map but absent in the WMAP combined map, i.e., spots 12~17, are near the Galactic plane. They should have been masked out by the Kp0 mask in the WMAP combined map even if they do exist. On the other hand, all the spots found in the Tegmark map at high latitudes, i.e., spots 3, 4 and 7, are all found



(a) The filtered combined WMAP map



(a) The filtered Tegmark map

(b) After 3σ thresholded(b) After 3σ thresholdedFIG. 3.— Inverse spherical wavelet transformed and 3σ thresholded Q-V-W-combined WMAP maps in real space.FIG. 4.— Inverse spherical wavelet transformed and 3σ thresholded Tegmark cleaned maps in real space.

in the *WMAP* combined map, whereas there are other high-latitude spots found in the combined map but absent in the Tegmark map, which we discuss later in the source determination that the Tegmark map seems to be “cleaner” than the *WMAP* combined map at some level. Indeed, we should be very cautious of these spots, especially those near the Galactic plane. Whether they are true or not needs further investigation. We suggest that the spots at high latitudes are more real. These different-filtering spots may have something to do with varying noise weights used, or with foreground residuals, since the two maps have been processed using different foreground removal techniques. However, we discuss the possible sources of this non-Gaussianity in detail below. We have carried out the analysis after the spots are removed from the maps, and there is indeed no significant deviation from Gaussian fluctuations, indicating these spots do contribute to the detected non-Gaussianity. Note that spot 7 corresponds to the cold spot pointed out in Vielva *et al.* (2004) and further discussed in Cruz *et al.* (2005); the deep hole corresponding to spots 15, 16, and 17 is also present in the *WMAP* internal linear combination map and does not fail a Minkowski functional analysis (Colley & Gott 2003) in which some non-Gaussian features are more sensitive in wavelet spaces than in others.

TABLE 2. COORDINATES OF THE FILTERED NON-GAUSSIAN SPOTS. THE NUMBER OF STANDARD DEVIATIONS THE SPOT DEVIATE FROM THE MEAN ARE GIVEN BY N_σ . THE SPACE MEANS THE SPOT IS NOT DETECTED IN THE SPECIFIC MAP.

No.	The WMAP combined			The Tegmark cleaned		
	b	l	N_σ	b	l	N_σ
1	40°	245°	-3.12			
2	-34°	79°	-3.06			
3	-31°	157°	-3.08	-31°	157°	-3.11
4	-47°	174°	3.20	-47°	174°	3.06
5	-29°	218°	-3.15			
6	-54°	180°	3.28			
7	-58°	210°	-3.23	-58°	210°	-3.09
8	-14°	322°	-3.69			
9	-20°	340°	-3.14			
10	-23°	348°	-3.09			
11	-43°	342°	-3.06			
12				-8°	182°	-3.28
13				-10°	199°	-3.35
14				-21°	264°	3.38
15				-7°	318°	-4.01
16				-11°	323°	-3.76
17				-10°	331°	-3.49

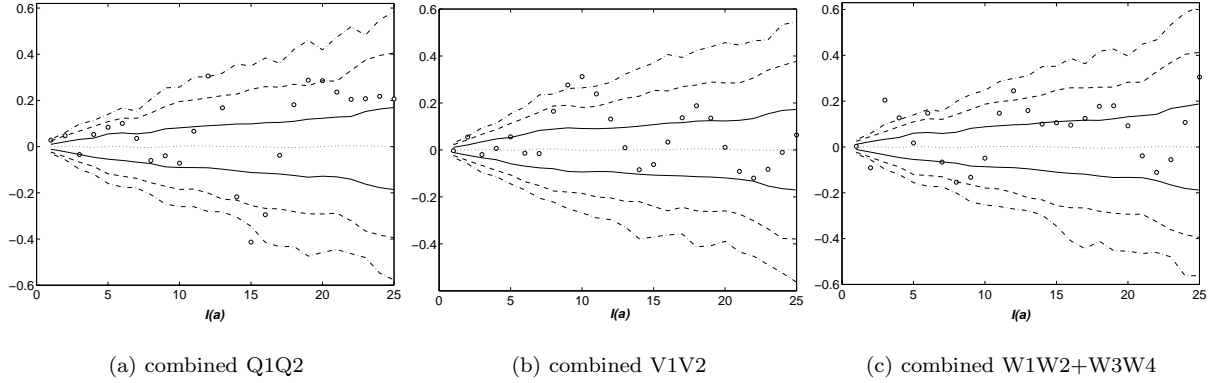


FIG. 5.— Skewness values obtained from the analysis of different receiver combinations, where the CMB and foreground contributions are negligible, shown as circles. Note that they all seem to be compatible with Gaussian simulations at the scales at which the non-Gaussianity is detected and exhibit very different patterns from those of the CMB maps, indicating that systematic effects due to beams do not significantly contribute to the detected non-Gaussianity.

4.3. Sources of Non-Gaussianity

We perform analysis in the wavelet space using SMW to discuss the sources of the detected non-Gaussianity. Vielva *et al.* (2004) have studied this issue using isotropic SMHW and concluded that systematics, foregrounds, and noise can be rejected as the source, except for possible intrinsic fluctuations. Here we re-examine the possible sources of the detected non-Gaussianity.

We subtract maps of the receivers at the same frequency to produce maps almost free from CMB and foreground. These maps include possible systematic instrumental features like the beams and noise of each band. SMW analysis has been performed, and the skewnesses with confidence levels obtained from individual Monte Carlo simulations of each band are shown in Fig. 5. They do not show significant non-Gaussian fluctuations and exhibit completely different patterns from the skewness curve obtained from the Q-V-W-combined map. Note that Q-band has 99% outliers at $l(a) \sim 12$ and ~ 15 , V-band at ~ 10 , and W-band at ~ 3 and ~ 4 . Thus, both Q and V channels show some deviations around the scales where the non-Gaussianity is detected. However, they are not significant enough to explain the detected deviations, which achieve their maxima around $l(a) \sim 11$ in all three bands. The numbers of deviations and the corresponding significance levels are displayed in Table (3). In addition, we have tested this by adding an over-estimated noise contamination supplied by the WMAP team to Gaussian CMB simulations, but the detected non-Gaussian signal does not appear in the analysis.

We also examine each receiver by performing the analysis on the Q1, Q2, V1, V2, W1, W2, W3, and W4 maps. The skewnesses with confidence levels from Gaussian simulations are shown in Fig. 6(a). They all exhibit a pattern similar to the combined WMAP map; thus, the deviations are not caused by any particular receiver. These tests indicate that systematic effects do not contribute significantly to the detected non-Gaussianity.

For the possible contribution of foreground to the detected non-Gaussianity, we note that it can be categorized into two parts: one is from the foreground emission templates adopted by the WMAP team and another is

TABLE 3. DEVIATIONS AND SIGNIFICANCE LEVELS OF SEVERAL OUTLYING SPHERICAL WAVELET COEFFICIENT STATISTICS OBTAINED FROM ANALYZING DIFFERENT RECEIVER COMBINATIONS, WHERE THE CMB AND FOREGROUND CONTRIBUTIONS ARE NEGLIGIBLE. SIGNIFICANT LEVELS ARE CALCULATED FROM 10,000 GAUSSIAN SIMULATIONS. THE NUMBER OF STANDARD DEVIATIONS THE OBSERVATION DEVIATES FROM THE MEAN IS GIVEN BY N_σ ; THE CORRESPONDING SIGNIFICANCE LEVEL OF THE DETECTED NON-GAUSSIANITY IS GIVEN BY δ .

Q1Q2			V1V2			W1W2+W3W4		
I(a)	N_σ	δ	I(a)	N_σ	δ	I(a)	N_σ	δ
12	3.0	99.2%	9	3.0	99.4%	2	-4.0	99.9%
15	-3.3	99.5%	10	3.4	99.6%	3	5.8	>99.9%
						4	2.9	99.3%

some possible residual contamination after foreground-template correction. We check the former by (1) analyzing a map almost free of CMB signals; the map is made by subtracting the two receivers of Q band and the two receivers of V band from the four receivers of W band. This map will contain significant contributions from foregrounds and noise derived from the WMAP data (Vielva *et al.* 2004). The skewness of this map and its own confidence levels from Monte Carlo simulations are shown in Fig. 7(a), showing very different patterns of that from the cleaned map (Fig. 6(a)), and no significant deviations from Gaussian fluctuations are seen. (2) We also analyze the statistical properties of the foreground templates obtained by the WMAP team by adding overestimated foreground contaminations to a simulated Gaussian CMB map. The skewness of these maps and their corresponding confidence levels are shown in Fig. 7(b), where the detected non-Gaussian signal does not appear, indicating no correlation with Galactic foregrounds. In addition, since the non-Gaussian signals are detected at intermediate scales, the foreground emission templates can be excluded as the source of the detected non-Gaussianity.

We now examine the latter possibility. Although skewness values obtained from all receivers present very similar patterns, they show some frequency dependence in Fig. 6. The deviation numbers of each receiver and the corresponding significance levels from simulations of each

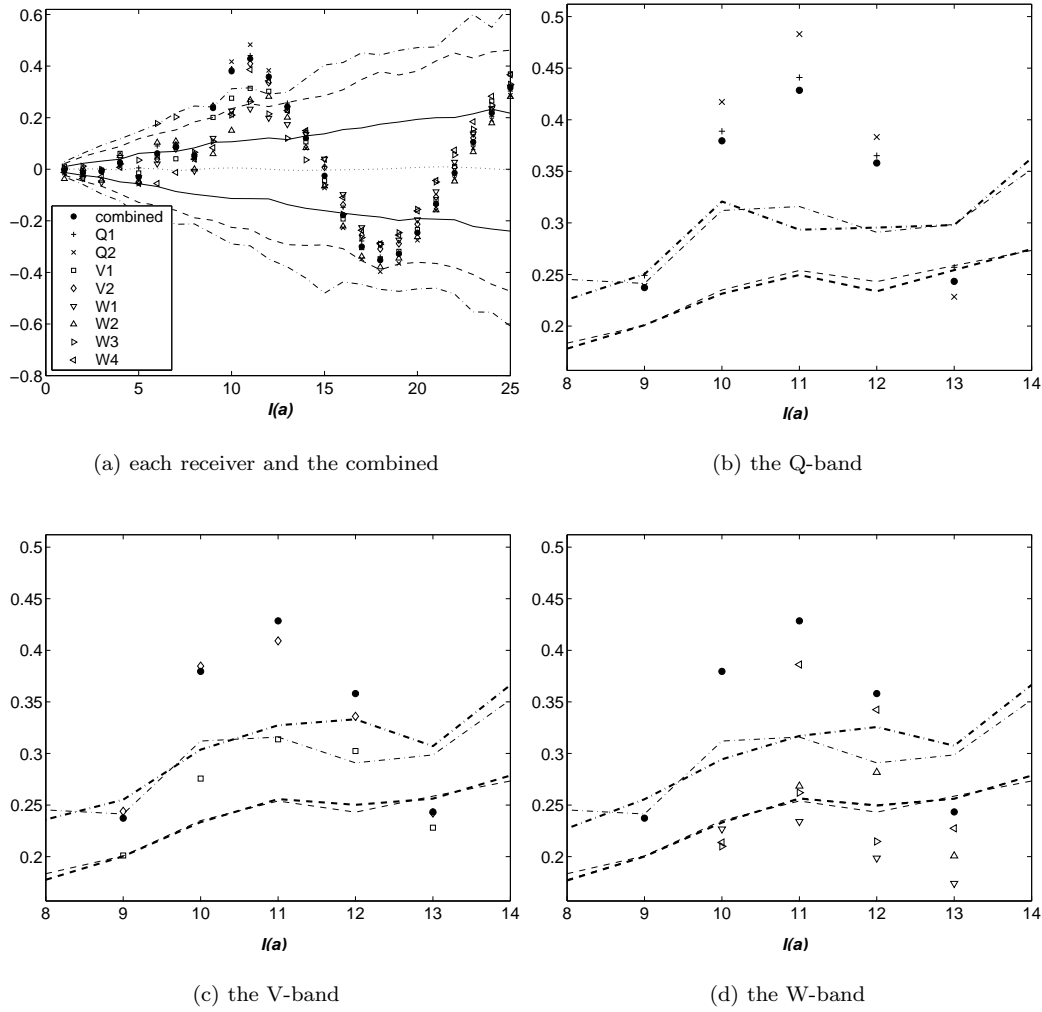


FIG. 6.— Skewness values obtained from the analysis of each WMAP receiver. Panel (a) shows that all receivers exhibit a similar pattern with that of the combined map, indicating the non-Gaussianity is not caused by any particular receiver. However, the level of deviations are different for different bands; this is shown more clearly in (b), (c) and (d) which presents a magnified part of (a) separately from each band at scales of interest in this work. Since the noise and beams vary at some level among different receivers, we also carry out Monte Carlo simulations separately for each band. The heavy lines represent the confidence levels of each band, whereas the light lines show the confidence levels of the Q-V-W combined data as the same as those in (a) for a comparison. The W -band deviates less than the V -band, which deviates less than the Q -band, indicating the existence of some frequency-dependent signals that are most likely from the residual foreground contaminations. Note that Q -band is particularly suspected.

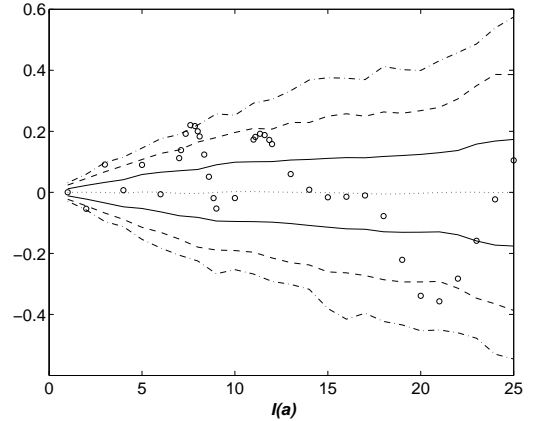
TABLE 4. DEVIATIONS AND SIGNIFICANCE LEVELS OF SPHERICAL WAVELET COEFFICIENT STATISTICS OBTAINED FROM ANALYZING EACH- RECEIVER MAPS OF THE WMAP. SIGNIFICANT LEVELS ARE CALCULATED FROM 10,000 GAUSSIAN SIMULATIONS SEPARATELY OF EACH BAND. THE NUMBER OF STANDARD DEVIATIONS THE OBSERVATION DEVIATES FROM THE MEAN IS GIVEN BY N_σ ; THE CORRESPONDING SIGNIFICANCE LEVEL OF THE DETECTED NON-GAUSSIANITY IS GIVEN BY δ .

I(a)	10		11		12	
Receiver	N_σ	δ	N_σ	δ	N_σ	δ
Q1	3.4	99.9%	3.6	>99.9%	2.9	99.5%
Q2	3.7	>99.9%	4.0	>99.9%	3.0	99.6%
V1	2.4	98.6%	2.5	98.9%	2.3	97.7%
V2	3.4	99.9%	3.3	99.9%	2.6	98.8%
W4	1.9	94.0%	3.1	99.8%	2.7	98.8%

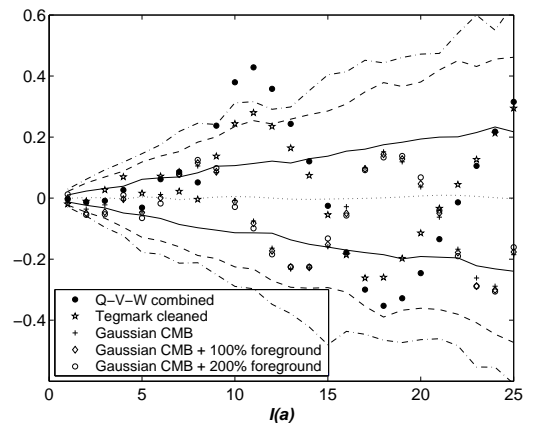
band are displayed in Table (4). Although in one particular band, there are differences in the relative amplitudes of each receivers, we may find a systematic trend in frequency dependence among the three bands. Skewness of Q -band deviates more than that of V -band, which also deviates more than that of W -band. We have verified that these different levels of deviations from Gaussian fluctuations are not caused by the different measurement noises of these receivers at different frequencies. The beams and noise have been calibrated out with simulations of each individual band. The slight differences in relative amplitudes from receivers of one particular band may be due to subtle interplay between the instrument behavior and foregrounds. If the central frequency of two receivers of the same band differ from each other, then different levels of foregrounds could remain in the different channels. Note that W -band would be the band least contaminated with foreground synchrotron and free-free emissions, and dust emissions has not reached its maximum at the W-band frequency. We can take a rough quantitative comparison of total foreground components among the three bands by using Fig. 10a in Bennett *et al.* (2003b). This figure shows that V -band and W -band would be cleaner than Q -band if foreground residuals exist and that W -band would be the cleanest, particularly if synchrotron-related foreground residuals exist. Moreover, Fig. 7(b) shows that the skewness of the Tegmark cleaned map exhibits less deviations from Gaussianity than the combined WMAP map, perhaps due to more complete foreground removal in the Tegmark map. Meanwhile, if the non-Gaussianity is totally due to the intrinsic temperature fluctuations, there is no reason why the deviations should be different at different frequencies and also different between the WMAP team-recommended map and the Tegmark map. In addition, noise properties cannot explain features among different scale ranges. It might be true that due to different noise properties the deviations in the combined WMAP map and the Tegmark cleaned map vary with each other on small scales ($a_1 \sim a_6$). But on medium scales $a_8 \sim a_{14}$, in which range the non-Gaussianity has been detected, values of the WMAP map are systematically larger than those of the Tegmark map. So if we believe that the Tegmark map is cleaner than the WMAP map, the foreground residual explanation is natural. We therefore conclude that the most likely source of the detected non-Gaussianity is the residual foreground signals in the map. As a cautious note, we cannot completely exclude the intrinsic CMB signal in this work as the source of the detected non-Gaussianity, since we have not determined the exact nature of the possible foreground residual and quantified its contribution to the non-Gaussianity systematically. Whether this non-Gaussianity is due to foreground residuals or due to intrinsic signals is still an open issue. Nevertheless, we have shown several independent arguments for possible foreground residuals, so it is highly likely that they are at least a promising candidate for the source of the detected non-Gaussianity.

5. CONCLUSIONS AND DISCUSSIONS

We have performed spherical wavelet analysis on the WMAP first-year data and detected non-Gaussianity in wavelet space and localized some non-Gaussian spots in



(a) foregrounds and noise component



(b) the combined, the Tegmark cleaned and a Gaussian CMB simulation with overestimated contamination

FIG. 7.— Skewness values from the analysis of (a), foregrounds and noise component that is almost free of CMB emission, and (b), distinctly foreground-removed and overestimated WMAP-foreground-template contaminated maps. Panel (a) shows concordance with the Gaussian simulation and a different pattern from the CMB maps, indicating that the foreground component in the WMAP map does not contribute significantly to the detected non-Gaussianity. Panel (b) shows that the detected non-Gaussianity does not appear when adding to a Gaussian CMB simulation one and two times WMAP-foreground-template contaminations; deviations of the Tegmark map are less than those of the WMAP map, indicating some dependence on foreground removal technique, which could be caused by unresolved residual foreground.

real space. In wavelet space, deviations from Gaussianity are found in skewness on scales from $\sim 11^\circ$ to $\sim 14^\circ$, on the sky with a maximum around 12° , and in kurtosis on scales smaller than $\sim 11^\circ$, with a maximum around 9° toward azimuthal orientation $\varphi_0 \sim 0^\circ$, using anisotropic SMW. Several possible non-Gaussian spots are detected in real space using isotropic SMHW from both the Q-V-W-combined WMAP map and the Tegmark cleaned map. We have also investigated the possible sources of this detected non-Gaussianity in detail.

Systematic effects have been excluded, because (1) the skewness of the maps including possible systematic in-

strumental features do not show significant deviations from Gaussian fluctuations at the scales where the non-Gaussianity is detected and (2) the skewness is different at different frequencies and they all show very different patterns from the CMB maps. To be stricter, there still might be the possibility that some of the observations were due to unknown systematic effects. Although we refer to different maps at the same frequency as evidence of lack of systematics, this does not exclude common-mode systematic artifacts. Foreground templates adopted by the *WMAP* team also make no significant contribution, because (1) the maps with significant contributions from foregrounds and noise derived from the *WMAP* data do not show significant deviations from Gaussian fluctuations and exhibit very different patterns from CMB signals and (2) maps containing overestimated *WMAP*-derived foreground template signals show no deviation from Gaussianity. We find in several independent ways that the level of non-Gaussianity is correlated positively with the level of possible foreground contaminations due to incomplete foreground removal. Among the three bands, Q -band seems to be the most contaminated, probably due to residual synchrotron emission. We conclude that the most likely source of the detected non-Gaussianity is residual foreground signals in the map.

Although the *WMAP* team do not include the Q-band channels in any power spectrum computations for $l < 100$, which overlaps the scales where the non-Gaussianity is detected, we want to remark that the non-Gaussian features are also seen when excluding Q -band. Individual band results primarily show that Q -band contributes more to the non-Gaussianity than V and W bands, which

is reasonable for foreground residuals, since emissions are dominant at some bands and minor at others. Therefore, it is still premature to do more precise tests on the non-Gaussianity of the intrinsic CMB fluctuations before we can identify the origin of these foreground signals, understand their nature, and finally remove them from the CMB maps completely. We will investigate the origin of the detected non-Gaussian signals in our future work and also look forward to the *WMAP* second-year data for confirming these results and detecting these non-Gaussian signals more precisely.

Acknowledgement: The authors kindly thank J. Laurent for very useful help on the use of the YAWtb toolbox and M. Tegmark for guidance on the weights of the Tegmark cleaned map. We are very grateful to the anonymous referee whose extremely detailed and insightful comments and suggestions allowed us to clarify several issues and improve the readability of the paper. We acknowledge the use of the LAMBDA. Support for LAMBDA is provided by the NASA Office of Space Science. This work has used the software package HEALPix (hierarchical, equal area and iso-latitude pixelization of the sphere, <http://www.eso.org/science/healpix>), developed by K.M. Gorski, E. F. Hivon, B. D. Wandelt, J. Banday, F. K. Hansen and M. Barthelmann. This research has made use of the Astrophysical Integrated Research Environment (AIRE) which is operated by the Center for Astrophysics, Tsinghua University. This study is supported in part by the Special Funds for Major State Basic Research Projects, by the Directional Research Project of the Chinese Academy of Sciences and by the National Natural Science Foundation of China.

REFERENCES

- Aghanim, N., Forni, O. & Bouchet, F.R. 2001, *A&A*, 365, 341
 Antoine, J.-P., & Vanderghyest, P. 1998, *J. Math. Phys.*, 39, 3987
 Bardeen, J. M., Bond, J. R., Kaiser, N., Szalay, A. S. 1986, *ApJ*, 304, 15
 Bardeen, J. M., Steinhardt, P. J., Turner, M. S. 1983, *Phys. Rev. D*, 28, 679
 Barreiro, R. B., *et al.* 2000, *MNRAS*, 318, 475
 Bennett, C. L., *et al.* 2003a, *ApJS*, 148, 1
 Bennett, C. L., *et al.* 2003b, *ApJS*, 148, 97
 Bogdanova, I., Vanderghyest, P., Antoine, Jean-Pierre, Jacques, L., & Morvidone, M. References Proc. EUSIPCO 2004 (Vienna, Sept. 2004), vol. 1, pp. 49–52
 Bond, J. R., Efstathiou, G. 1987, *MNRAS*, 226, 655
 Cayón, L., Sanz, J. L., Martínez-González, E., Banday, A. J., Argüeso, F., Gallegos, J. E., Górski, K. M., & Hinshaw, G. 2001, *MNRAS*, 326, 1243
 Cayón, L., Martínez-González, E., Argüeso, F., Banday, A. J., & Górski, K. M. 2003, *MNRAS*, 339, 1189
 Chiang, L. -Y., Naselsky, P. D., Verkhodanov, O. V., Way, M. J., 2003, *ApJ*, 590, L65
 Chiang, L.-Y., & Naselsky, P. D. 2004, *astro-ph/0407395*
 Coles, P., Dineen, P., Earl, J., Wright, D. 2004, *MNRAS*, 350, 989
 Colley, W. N., & Gott, J. R. 2003, *MNRAS*, 344, 686
 Cruz, M., Martínez-González, E., Vielva, P., & Cayón, L. 2005, *MNRAS*, 356, 29
 Eriksen, H. K., Hansen, F. K., Banday, A. J., Gorski, K. M., Lilie, P. B. 2004a, *ApJ*, 605, 14
 Eriksen, H. K., Novikov, D. I., Lilie, P. B., Banday, A. J., Gorski, K. M. 2004b, *ApJ*, 612, 64
 Finkbeiner, D. P. 2003, *ApJS*, 146, 407
 Finkbeiner, D. P., Davis, M., & Schlegel, D. J. 1999, *ApJ*, 524, 867
 Górski, K. M., Hivon, E., Wandelt, B. D. 1999, *astro-ph/9812350*
 Guth, A. H., Pi, S.-Y. 1982, *Phys. Rev. Lett.*, 49, 1110
 Hansen, F. K., Cabella, P., Marinucci, D., Vittorio N. 2004, *ApJ*, 607, L67
 Haslam, C. G. T., Salter, C. J., Stoffel, H., & Wilson, W. E. 1982, *A&AS*, 47, 1
 Hawking, S. W. 1982, *Phys. Lett. B*, 115, 295
 Hinshaw, G., *et al.* 2003, *ApJS*, 148, 63
 Hinshaw, G., *et al.* 2003, *ApJS*, 148, 135
 Hobson, M. P., *et al.* 1999, *MNRAS*, 309, 125
 Komatsu, E., *et al.* 2003, *ApJS*, 148, 119
 Larson D. L., & Wandelt, B. D. 2004, *ApJ*, 613, L85
 Martínez-González, E., *et al.* 2002, *MNRAS*, 336, 22
 McEwen, J. D., *et al.* 2005, *MNRAS*, 359, 1583
 Mukherjee, P., Hobson, M.P., & Lasenby, A. N. 2000, *MNRAS*, 318, 1157
 Mukherjee, P., & Wang, Yun 2004, *ApJ*, 613, 51
 Naselsky, P. D., Doroshkevich, A. G., Verkhodanov, O. V. 2003, *ApJ*, 599, L53
 Naselsky, P. D., Doroshkevich, A. G., Verkhodanov, O. V. 2004, *MNRAS*, 349, 695
 Pando, J. Valls-Gabaud, D., Fang, L. Z. 1998, *Phys. Rev. Lett.*, 81, 4568
 Park, C.-G. 2004, *MNRAS*, 349, 313
 Schlegel, D. J., Finkbeiner, D. P., & Davis, M. 1998, *ApJ*, 500, 525
 Seljak, U., & Zaldarriaga, M. 1996, *ApJ*, 469, 437
 Spergel, D. N., *et al.* 2003, *ApJS*, 148, 175
 Tegmark, M., de Oliveira-Costa, A., & Hamilton, A. J. S. 2003, *Phys. Rev. D*, 68, 123523
 Tenorio, L., Jaffe, A. H., Hanany, S., & Lineweaver, C. H. 1999, *MNRAS*, 310, 823
 Vielva, P., *et al.* 2004, *ApJ*, 609, 22
 Wibig, T. & Wolfendale, A. W. 2005, *MNRAS*, 360, 236